2020

Anti-Resonance, Inhibited Coupling and Mode Transitionin Depressed Core Fibers

XIAOKANG LIAN

Gerald Farrell

QIANG WU

See next page for additional authors

Authors

XIAOKANG LIAN, Gerald Farrell, QIANG WU, Wei Han, CHANGYU SHEN, YOUQIAO MA, and Yuliya Semenova

Anti-resonance, inhibited coupling and mode transition in depressed core fibers

Article *in* Optics Express · April 2020

DOI: 10.1364/OE.390371

CITATIONS
2

READS
160

7 authors, including:

Xiaokang Lian
Technological University Dublin - City Campus
17 PUBLICATIONS **74** CITATIONS
SEE PROFILE

Gerald Farrell
Technological University Dublin
441 PUBLICATIONS **5,551** CITATIONS
SEE PROFILE

Qiang Wu
Northumbria University
313 PUBLICATIONS **2,885** CITATIONS
SEE PROFILE

Wei Han
Technological University Dublin - City Campus
18 PUBLICATIONS **102** CITATIONS
SEE PROFILE

Anti-resonance, inhibited coupling and mode transition in depressed core fibers

XIAOKANG LIAN,[1,*] GERALD FARRELL[1], QIANG WU,[2] WEI HAN,[1] CHANGYU SHEN,[3] YOUQIAO MA,[4] AND YULIYA SEMENOVA[1]

[1]*Photonics Research Centre, Technological University Dublin, Dublin D08 X622, Ireland*
[2]*Department of Mathematics, Physics, and Electrical Engineering, Northumbria University, Newcastle upon Tyne NE1 8ST, U.K.*
[3]*Institute of Optoelectronic Technology, China Jiliang University, Hangzhou 310018, China*
[4]*School of Physics and Optoelectronic Engineering, Nanjing University of Information Science and Technology, Nanjing, 210044, China.*
**d15128010@mytudublin.ie*

Abstract: The depressed core fiber (DCF), consisting of a low-index solid core, a high-index cladding and air surrounding, is in effect a bridge between the conventional step-index fiber and the tube-type hollow-core fiber from the point of view of the index profile. In this paper the dispersion diagram of a DCF is obtained by solving the full-vector eigenvalue equations and analyzed using the theory of anti-resonant and the inhibited coupling mechanisms. While light propagation in tube-type hollow-core fibers is commonly described by the symmetric planar waveguide model, here we propose an asymmetric planar waveguide for the DCFs in an anti-resonant reflecting optical waveguide (ARROW) model. It is found that the anti-resonant core modes in the DCFs have real effective indices, compared to the anti-resonant core modes with complex effective indices in the tube-type hollow-core fibers. The anti-resonant core modes in the DCFs exhibit similar qualitative and quantitative behavior as the core modes in the conventional step-index fibers. The full-vector analytical results for the simple-structure DCFs can contribute to a better understanding of the anti-resonant and inhibited coupling guidance mechanisms in other complex inversed index fibers.

1. Introduction

Inversed index fibers with a low-index core and a high-index cladding such as the tube-type hollow-core fibers and hollow-core photonic crystal fibers have attracted a lot of interest in the fields of high-capacity telecommunication networks [1-5], high-power/supercontinuum/ultrafast lasers [6-11], terahertz waveguiding [12,13] and high sensitivity optical sensing [14,15]. As opposed to conventional step-index fibers where the light is guided in the high-index core region by total internal reflections, light guidance in the low-index core region of the inversed index fibers can be explained by other mechanisms such as the photonic bandgap effect, inhibited coupling effect and the anti-resonant effect. Generally, all optical fibers can be grouped into two types based on the effective refractive index (n_{eff}) - wavelength (λ) dispersion diagram [2]. For the first type, the n_{eff} - λ of the core modes lies outside any cladding mode continuum. The photonic bandgap fibers belong to this type, as their photonic bandgaps are formed in the periodic dielectric cladding region, the coupling between the core modes, which have n_{eff} within the bandgaps, and cladding modes are forbidden due to their separation in the n_{eff} - λ space [3]. The second type is inhibited coupling fibers, for which the n_{eff} - λ of the core modes lies inside the cladding mode continuum, but the coupling between them is minimized due to the high degree of transverse-field mismatch [6]. Both the photonic bandgap fibers and the inhibited coupling fibers have the same anti-resonant nature, which can be described by an anti-resonant reflecting optical waveguide (ARROW) model [2,3,6]. In this

model, the planar waveguide acts as a Fabry-Perot resonator, which allows the anti-resonant light to be reflected back while allowing forward transmission of the resonant light [16-19].

In a manner similar to photonic bandgap fibers, conventional step-index fibers belong to the first type since the n_{eff} of the core modes are higher than that of the cladding modes, in other words, their modal dispersion space is separated [2]. Compared to conventional step-index fibers, inversed index fibers have generally a more complex structure and modal characteristics. However, there exists a close relationship between them. It has been stated that the photonic bandgap fibers exhibit strikingly similar modal behavior with that of the conventional fibers, including dispersion curves and field profiles [20,21]. The analogy to conventional fibers provides a convenient tool to model the modes of photonic bandgap fibers. The question is whether there is a connection between the inhibited coupling fibers and the conventional fibers in addition to the photonic bandgap fibers.

A recent publication Ref. [22] shows that the mode density of anti-resonant elements in an inhibited coupling guiding single-ring hollow-core photonic crystal fiber is similar to the behavior of conventional multimode fibers. The single-ring hollow-core photonic crystal fiber studied in [22] has a ring of 6-8 detached thin tube-type hollow-core waveguides/fibers surrounding the hollow core. However, the results of the work were obtained using a scalar semi-analytical model, which does not give sufficiently rigorous vector modal analysis. The tube-type hollow-core fiber has a simple structure, where the leaky core-type modes are supported by the anti-resonant effect [17-19]. In most of the previous works, only the fundamental mode or few low-order modes of the tube-type hollow-core fibers were obtained with different approximation methods [17,23-25].

A depressed core fiber (DCF) is a type of inversed index fibers, described by a three-layer fiber model with a low-index solid core, a finite high-index cladding, and surrounding air. This fiber structure is different from the M-type fiber [26], although in some papers it has been referred to as M-type fiber [27]. The refractive index of the central region of the M-type fiber has a minimum value set by the need for the core to have a refractive index equal to or lower than that of the surrounding medium, which if the surrounding region is air means that the core must also be air. For a DCF the core refractive index is lower than the next outermost region but does not need to take on the lowest or minimum value in a three-layer fiber model. The M-type fiber can be considered as a leaky waveguide with the anti-resonant structure, in which the core mode is leaky with a complex effective refractive index, similar to the case of the hollow-core fiber [17,28]. Compared to the M-type fiber, the core mode of the DCF is guided by both total internal reflection and anti-resonance guidance, and its core mode has a real effective refractive index [27,29-32]. The DCFs have been studied for various applications including pulse compression in fiber lasers [29-31], generation of supercontinuum [27] and top-hat beams [32], due to their manageable waveguide dispersion and exceptional modal field changes. However, these studies in regard to DCFs [27, 29-32] were limited to the analysis of a few modes in the strong dispersion region.

In this paper, the modal dispersion and field distributions of a DCF are calculated and analyzed with the vector field functions and eigenvalue equations for the three-layer fiber as given in [33-35]. To the best of our knowledge, it is the first report providing a complete vector modal dispersion diagram for the DCFs. In the section 2, the ray method is used to analyze the mode characteristics in the DCFs, in comparison to asymmetric planar waveguides. The possibility of anti-resonant core modes and the positions of the mode coupling (resonances) is analyzed using the ARROW model. In section 3, the dispersion curves and mode field distributions of the vector modes TE, TM, HE and EH are analyzed, along with their comparison for the case of conventional step-index fibers. It is found that the waveguiding mechanism of core-type modes in DCFs with a simple structure can be explained by the anti-resonant and inhibited coupling effects, similarly to the complex single-ring hollow-core photonic crystal fibers discussed in Ref. [22]. In section 4, the implications of the analytical results for the tube-type hollow-core fibers and single-ring hollow-core fibers are discussed.

2. Theory of the DCFs

Anti-resonant core mode and asymmetric planar ARROW model

Fig. 1 shows a DCF and its cross section and refractive index profile. The radii of the rod core and the tube cladding are r_1 and r_2 while the surrounding medium (air) is unlimited. The refractive index of the rod core region n_1 is smaller than the refractive index of the tube cladding region n_2 but greater than that of the surrounding air n_3, as $n_3 < n_1 < n_2$.

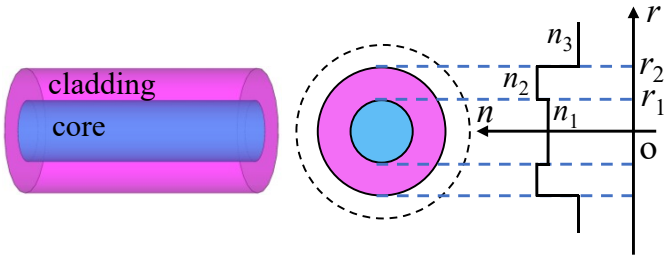

Fig. 1. A depressed-core optical fiber and its cross section and refractive index profile.

The high-index tube cladding region of the DCF can be considered as an asymmetric planar waveguide, where a high-index core region with the same thickness ($d = r_2 - r_1$) as the cladding of the DCF is sandwiched between two different low-index regions, as shown in Fig. 2. It is useful to analyze the DCFs using a ray optics approach. Since the asymmetric planar waveguide supports guided modes with $n_1 < n_{eff} = n_2 * \sin\theta_1 < n_2$ [36] shown in Fig. 2(b), it can be deduced that a DCF can support the annular-like (transverse field profile) cladding modes with $n_1 < n_{eff} = n_2 * \sin\theta_1 < n_2$ guided by the total internal reflections at the inner and outer boundaries of the cladding region as shown in Fig. 2(a). The modes with $n_3 < n_{eff} = n_1 * \sin\theta_1 < n_1$ in the asymmetric planar waveguide are radiation modes with power escaping into the higher-index (upper) region (where will form a standing wave field) [36], as shown in Fig. 2(d). In the DCF an incident ray representing a mode with $n_3 < n_{eff} = n_1 * \sin\theta_1 < n_1$, partially reflected at the inner boundary of the cladding region and totally reflected at the outer boundary of the cladding region, excites multiple path rays reflecting into the core region. The light field of these modes with $n_3 < n_{eff} < n_1$ is distributed in across the entire cross section of the DCF, which is similar to the cladding modes in conventional three-layer step-index fibers [37,38].

Due to the inversed index distribution in the DCF, the total internal reflection effect does not work at the inner boundary of the cladding region. Therefore, there is no core modes guided by the total internal reflections like those in conventional step-index fibers.

The high-index layers can be considered as Fabry-Perot resonators in the ARROW model [16]. Analogous to a symmetric planar waveguide in the ARROW model for the tube-type hollow-core fibers [18,19], an asymmetric planar waveguide is proposed for the DCFs. Indeed, the characteristics of multiple path reflections formed in the DCF shown in Fig. 2(c) indicate that the cladding region of the DCF acts as a Fabry-Perot resonator, corresponding to an asymmetric planar waveguide shown in Fig. 2(d). In a Fabry-Perot resonator the resonances usually occur over a narrow band of wavelengths while the antiresonances are spectrally broad [16,39]. The energy of the incident ray can be strongly reflected back to the core region at the anti-resonant wavelengths, forming anti-resonant core modes in the anti-resonant reflecting optical waveguides [16] and the tube-type hollow core fibers [18]. Similarly, it can be concluded that DCFs have anti-resonant core modes with the light field is mainly confined in the core region, with disc-like transverse field profiles.

The resonant wavelengths of an asymmetric planar waveguide-like Fabry-Perot resonator shown in Fig. 2(d), corresponding to the minimal total energy of all the reflected rays, are equal

to the cutoff wavelengths of the guided core modes. The cutoff wavelengths for the guided core modes TE_N and TM_N in the asymmetric waveguide can be written as [36]:

$$\lambda_{N,c} = \frac{2d\sqrt{n_2^2 - n_1^2}}{\left[N - 1 + \frac{1}{\pi}\tan^{-1}\left(\kappa\frac{\sqrt{n_1^2 - n_3^2}}{\sqrt{n_2^2 - n_1^2}}\right)\right]}, \quad \kappa = \begin{cases} 1, & \text{for } TE_N \text{ modes} \\ \frac{n_2^2}{n_3^2}, & \text{for } TM_N \text{ modes} \end{cases} \tag{1}$$

where N is the mode number. The second term in the denominator of Eq. (1) arises from the asymmetry of the waveguide and vanishes for the symmetric case as shown in Ref. [19].

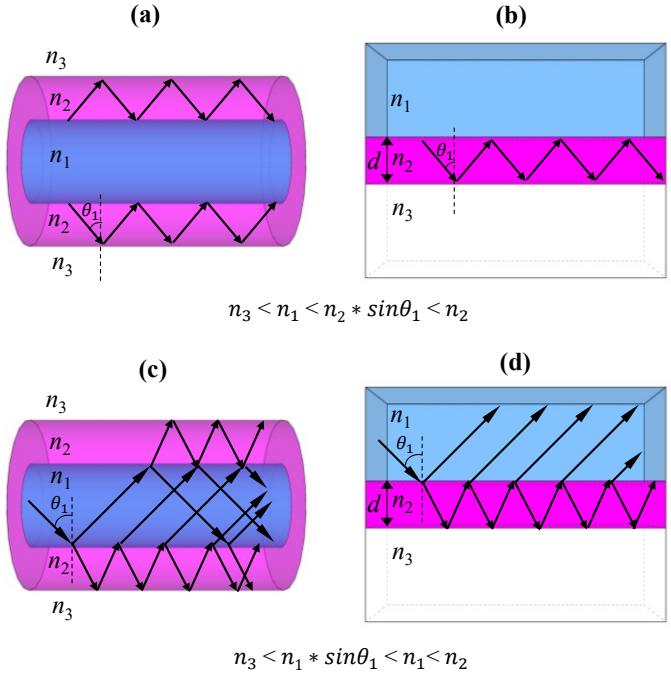

Fig. 2. (a) and (b) show the ray trajectory of a mode with $n_1 < n_{eff} = n_2 \sin\theta_1 < n_2$ in a DCF and an equivalent asymmetric planar waveguide, respectively. (c) and (d) show the ray trajectory of a mode with $n_3 < n_{eff} = n_1 \sin\theta_1 < n_1$ in the DCF and the equivalent asymmetric planar waveguide, respectively.

3. Results

Similar to the conventional step-index fibers, the modes in a DCF are denoted as $TE_{0,N}$, $TM_{0,N}$, $HE_{m,N}$ and $EH_{m,N}$, where the numbers '0' and 'm' on the left side of the comma in the subscript positions are the azimuthal mode number while the number symbols 'N' on the right side are the radial mode number. The eigenvalue equations for the vector modes in the DCFs are shown in Appendix, which were solved by a graphical method. In the calculations, the fiber parameters of the studied DCF are assumed as $n_1 = 1.445$, $n_2 = 1.51$, $n_3 = 1$, $r_1 = 62.5$ μm and $r_2 = 125$ μm. The parameters correspond to those of the fibers used in our experimental work, which will soon be presented in another paper.

3.1 TE/TM modes in DCFs

Fig. 3(a) shows the dispersion diagram (n_{eff} vs. λ) for the modes $TE_{0,N}$ with $n_1 < n_{eff} < n_2$. There are 38 $TE_{0,N}$ modes, from upper to lower as the radial mode number N increases, as indicated by the black arrow. All dispersion curves of the $TE_{0,N}$ modes with the purple dashed line at n_1,

but only the modes $TE_{0,N}$, N = 34, 35, 36, 37 and 38 have their cutoff in the investigated spectral range. The wavelengths of the intersect points are approximated as the cutoff wavelengths of the TE_N modes in the asymmetric planar waveguide calculated by Eq. (1), indicated by the red vertical dashed lines. The difference between the wavelength of the intersect point for the $TE_{0,N}$ mode and the cutoff wavelength of the TE_N mode is less than 1 nm. Compared to the curves above the horizontal line at n_1, the curves bellow n_1 show a step-like decrease as the λ increases, showing periodic strong and moderate index dispersion bands. The slopes of the dispersion curves with a strong index dispersion are similar to those of the curves above the horizontal line at n_1 and that in the equivalent asymmetric waveguide (not shown). The slopes of the dispersion curves with a moderate index dispersion in DCFs are similar to those of the dispersion curves of the core modes in the conventional step-index fiber, as discussed in part 3.3.

Fig. 3(c) shows the modal intensities and electric field vector distributions at seven different points marked A-G (black circle dots) in Figs. 3(a) and 3(b). The electric field vector helps to distinguish between different kinds of vector modes and helps to compare the modes in the DCF and the conventional step-index fiber, as discussed in following parts. The radial maxima in the modal field profiles represent intensity oscillations, and the number of the radial maxima is equal to the radial mode number N. In Fig. 3(c) the modal field profile of the mode $TE_{0,1}$ at point A shows one radial maxima in the fiber cladding region $r_1 < r < r_2$. The $TE_{0,2}$ at point B shows two radial maxima in the fiber cladding region.

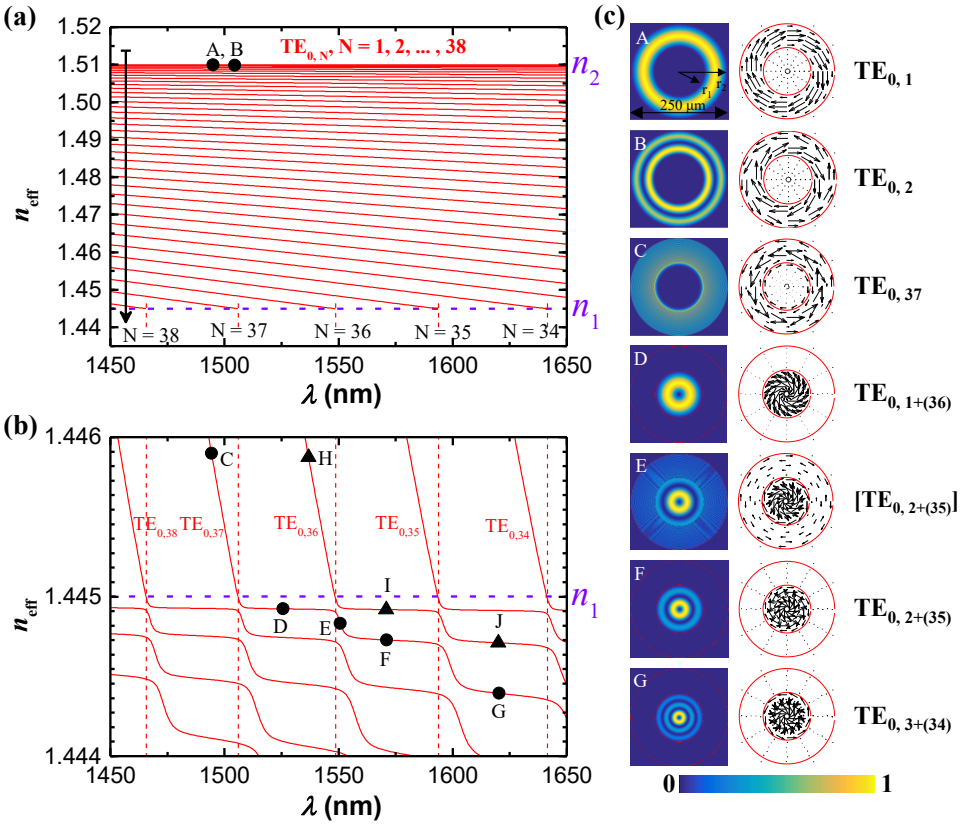

Fig. 3. Dispersion curves (n_{eff} vs. λ) of TE modes with n_{eff} corresponding to (a) $n_1 < n_{eff} < n_2$, (b) n_1-0.001 < $n_{eff} < n_1$+0.001, n_1 = 1.445, n_2 = 1.51. (c) shows the modal intensity and electric field vector distributions of TE modes whose positions (n_{eff}, λ) are indicated by the black circle dots in (a) and (b). The red vertical dashed lines in (a) and (b) indicate the resonant bands.

In order to count the number of radial maxima in the distributions corresponding to points C-G in Fig. 3(c), we draw the normalized intensity distribution along the *r*-coordinate, as shown in Fig. 4. One oscillation peak on a curve in Fig. 4 corresponds to one radial maxima in a modal field profile. Similar to the modal field profiles at points A and B, all 37 radial maxima are distributed within the fiber cladding region for the mode at point C. The oscillation peaks shift from the cladding region to core region one by one along the points C-G. The modes at points D, F and G exhibit 1, 2 and 3 maxima in the core and 36, 35 and 34 maxima in the cladding, respectively. The energy is mainly confined in the core region of the modes at points D, F and G, as seen in Figs. 4(b), 4(d) and 4(e), where the field intensity in the cladding region is almost negligible compared to that in the core region. The mode at point E with a very strong index dispersion represents a mode in a transition state from the mode at point D to the mode at point F, where the energy is more evenly distributed between the core and the cladding regions as seen in Fig. 4(c). There are 2 maxima in the core region and 35 maxima in the cladding region for the mode at point E.

We propose the following nomenclature for the modes with $n_{\text{eff}} < n_{1,}$ identified as $TE_{0,\,n+(N-n)}$. The subscript 'n' denotes the radial number in the core region, while the number 'N-n' denotes the radial number in the cladding region. Therefore, the modes at points D, F and G in Fig. 3(b) with moderate index dispersion can be named as $TE_{0,1+(36)}$, $TE_{0,2+(35)}$ and $TE_{0,3+(34)}$. The mode at point E in Fig. 3(b) can be named as $[TE_{0,2+(35)}]$, where the brackets indicate that the mode is with a strong effective index dispersion and is in a transition state. It is clear that the field profiles of the modes $TE_{0,1+(36)}$, $TE_{0,2+(35)}$ and $TE_{0,3+(34)}$ are similar to that of the modes $TE_{0,1}$, $TE_{0,2}$ and $TE_{0,3}$ in conventional step-index fibers, respectively. As discussed, the $TE_{0,1+(36)}$, $TE_{0,2+(35)}$ and $TE_{0,3+(34)}$ in the DCF should be formed by the anti-resonant effect of the high-index cladding region, therefore, they represent anti-resonant core modes.

According the above nomenclature, the modes at points I and J on the dispersion curve of $TE_{0,36}$ indicated by the black triangle dots in Fig. 3(b) are both anti-resonant core modes and named as $TE_{0,1+(35)}$ and $TE_{0,2+(34)}$, respectively. The mode transition from the core mode $TE_{0,1+(35)}$ at point I to the cladding mode $TE_{0,36}$ at point H and the mode transition from the higher-order core mode $TE_{0,2+(35)}$ at point F to the lower-order core mode $TE_{0,1+(36)}$ at point D leads to an anti-crossing phenomenon near the mode $[TE_{0,2+(35)}]$ at point E around the resonant bands indicated by the red vertical dashed line. Due to mode reorganization [38, 40-42], the anti-crossing phenomenon also takes place for the higher order modes. A similar phenomenon is also observed for the TM, HE and EH modes. The anti-crossing phenomenon originates from the resonant coupling between the core and the cladding modes, leading to the exceptional waveguide dispersion and modal field changes. As shown in Figs. 3 and 4 the modal field distribution and effective refractive index dispersion change drastically from the points D or F to the point E. The mode $[TE_{0,2+(35)}]$ at point E show similar strong dispersion with the cladding modes in the DCF and the modes in the equivalent asymmetric waveguide. Therefore, the wavelength position and the dispersion shape of the anti-crossing are related to the thickness and the refractive index of the high-index cladding, in accordance with the ARROW model and Eq. (1) as discussed in the theory section. Due to the manageable waveguide dispersion and modal field changes in a DCF, the generation of supercontinuum [27] and top-hat beams [32] can be achieved.

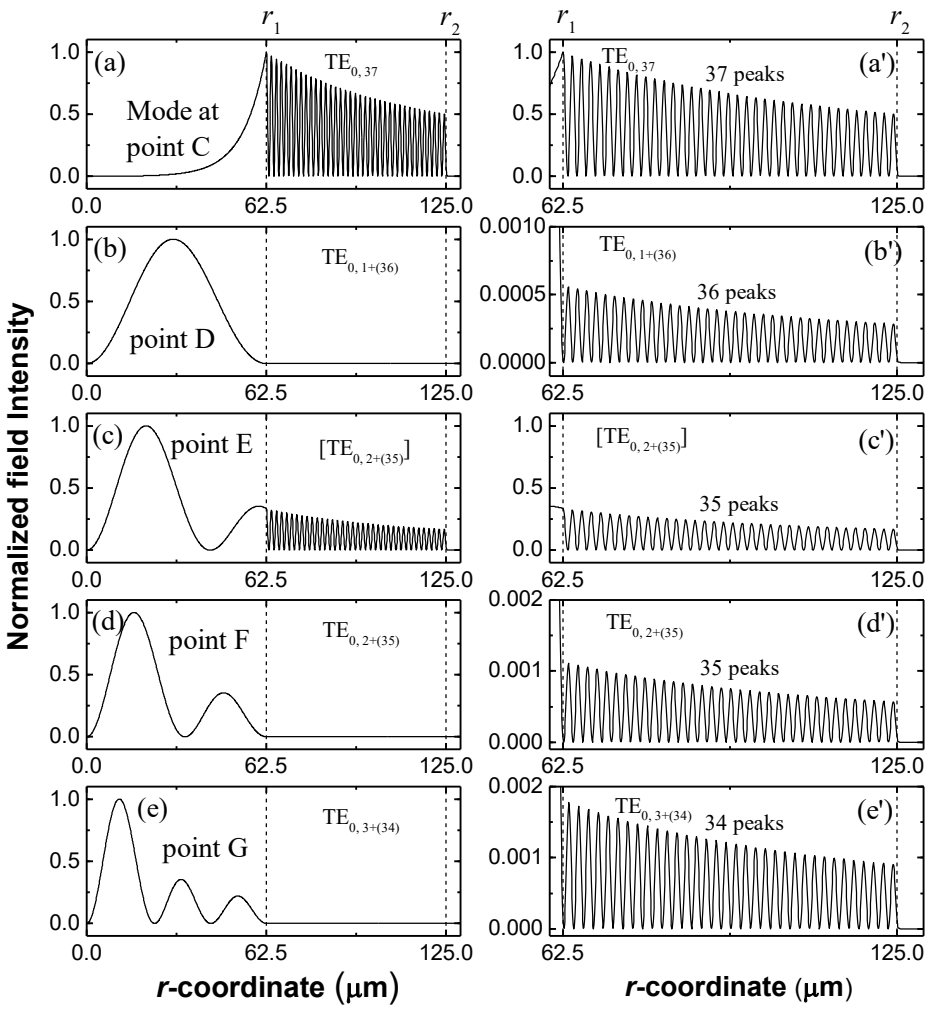

Fig. 4. The left panel (a)-(e) shows the normalized intensity distributions along the *r*-coordinate for the modes shown at points C-G in Fig. 3. The right panel (a')-(e') shows the zoomed-in part of (a)-(e), delineated by the vertical dashed lines.

The dispersion diagram of $TM_{0,N}$ modes is similar to that of $TE_{0,N}$ modes, as seen in Fig. 5. The positions of the intersect points between the dispersion curves of the $TM_{0,N}$ and the horizontal line at n_1 can be approximated as the cutoff wavelengths of the TM_N modes in the asymmetric planar waveguide calculated by Eq. (1), indicated by the black vertical dashed lines in Figs. 5(a) and 5(b). Fig. 5(c) shows the modal intensity and electric field vector distributions of TM modes at points A'-G' indicated by the black squares in Figs. 5(a) and 5(b). The modes at points A' and B' are $TM_{0,1}$ and $TM_{0,2}$, respectively. The points C'-G' are on the dispersion curve of $TM_{0,37}$. The field intensity distributions of TM modes in Fig. 5(c) are similar with those of TE modes shown in Fig. 3(c). However, the directions of the electric field vector of TM and TE modes are different: the former is parallel to the radial direction while the latter is normal in the radial direction.

Similarly to the nomenclature of the TE modes, the TM modes with $n_{eff} < n_1$ can be named as $TM_{0,n+(N-n)}$. Therefore, the anti-resonant core modes at points D', F' and G' in Fig. 5(b) with a moderate effective index dispersion can be named as $TM_{0,1+(36)}$, $TM_{0,2+(35)}$ and $TM_{0,3+(34)}$, respectively. The mode at point E' in Fig. 5(b) can be named as $[TM_{0,2+(35)}]$. From the modal

field distributions, it is clear that the anti-resonant core modes $TM_{0,1+(36)}$, $TM_{0,2+(35)}$ and $TM_{0,3+(34)}$ are similar to the core modes $TM_{0,1}$, $TM_{0,2}$ and $TM_{0,3}$ in the conventional step-index fibers, respectively.

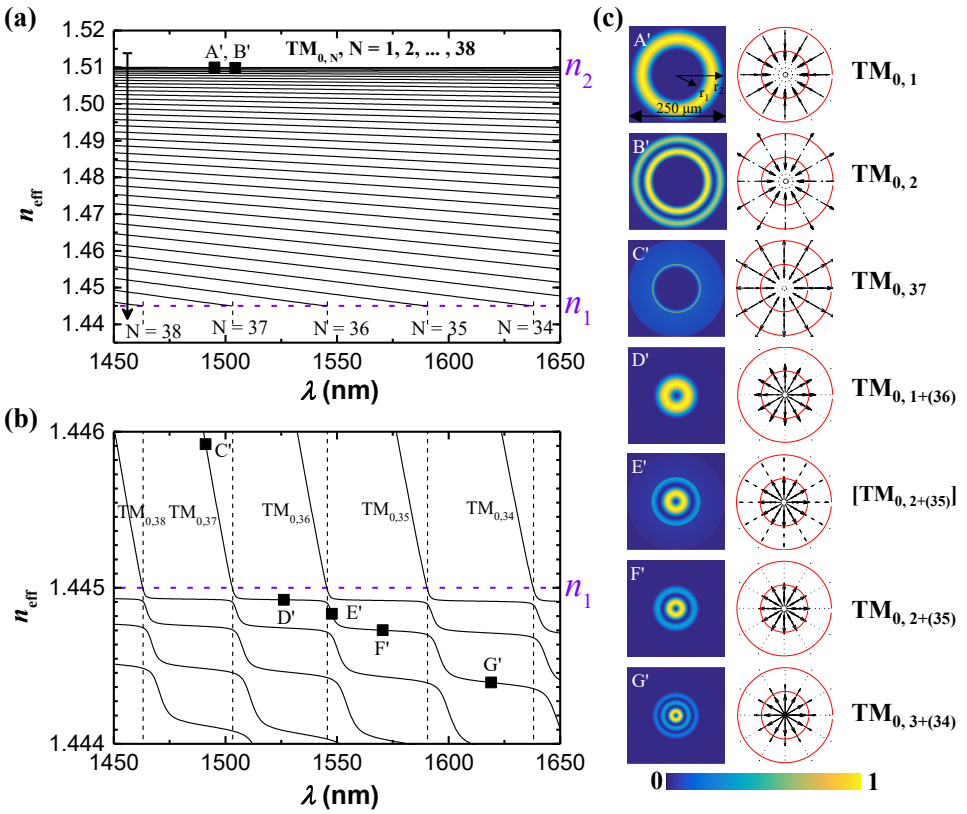

Fig. 5. Dispersion curves (n_{eff} vs. λ) of TM modes with n_{eff} corresponding to (a) $n_1 < n_{eff} < n_2$, (b) n_1-0.001 $< n_{eff} < n_1$+0.001, n_1 = 1.445, n_2 = 1.51. (c) shows the modal intensity and electric field vector distributions of TM modes whose positions (n_{eff}, λ) are indicated by the black squares in (a) and (b). The black vertical dashed lines in (a) and (b) indicate the resonant bands.

3.2 HE/EH modes in DCFs

The HE or EH in the DCFs are two-fold degenerate modes with the same effective refractive index but different field vector directions, similar to the HE/EH modes in conventional step-index fibers. Here we only show the results for one of these two-fold degenerate modes.

Fig. 6 illustrates the dispersion curves of the modes $HE_{1,N}$ and $EH_{1,N}$ (N = 34, 35,…, 38). Similar with the TE and TM modes in Figs. 3(b) and 5(b), the n_{eff} of $HE_{1,N}$ and $EH_{1,N}$ decrease linearly with the increase of λ when $n_{eff} > n_1$ while bellow n_1 the n_{eff} decrease in a step-like fashion as λ increases. The curves show periodic strong and moderate index dispersion bands. The positions of the intersect points between the dispersion curves of modes $HE_{1,N}$ ($EH_{1,N}$) and the horizontal line at n_1 can be approximated as the cutoff wavelengths of the TE_N (TM_N) modes in the asymmetric planar waveguide calculated by Eq. (1), indicated by the red (black) vertical dashed lines in Fig. 6.

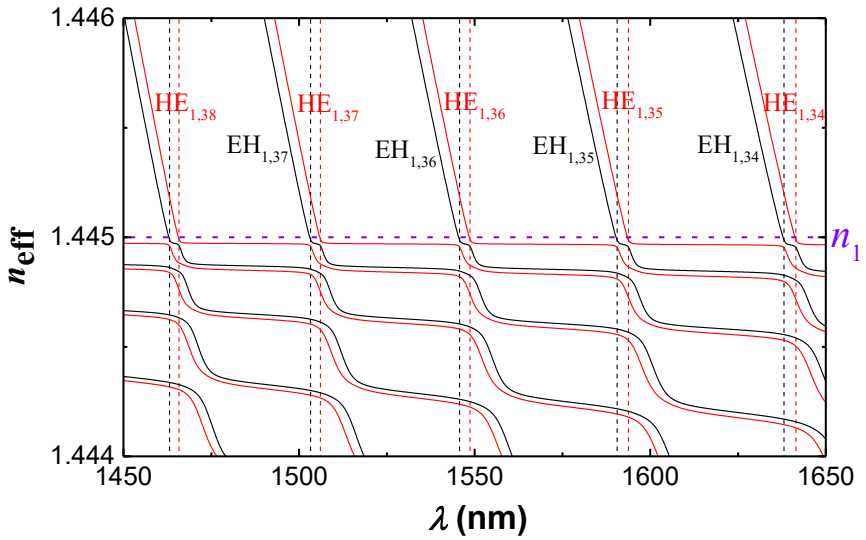

Fig. 6. Dispersion curves (n_{eff} vs. λ) of $HE_{1,N}$ (red) and $EH_{1,N}$ (black) modes with n_{eff} corresponding to (n_1-0.001 < n_{eff} < n_1+0.001, n_1 = 1.445. The black and red vertical dashed lines indicate the resonant bands.

For $HE_{m,N}$ or $EH_{m,N}$ modes, each radial mode order 'N' supports a larger number of azimuthal mode orders 'm'. Fig. 7(a) as an example shows a dispersion diagram of the $HE_{m,N}$ modes with m = 1, 2, … and N = 34, 35, …, 38. The curves with the same radial mode order 'N' are shown in the same color. For the sake of clarity, the transparency of the curves has been increased toward higher azimuthal mode orders in each group. All these curves form a very dense dispersion diagram, where the curves with moderate slopes intersect with those having steeper slopes.

Fig. 7(b) shows the zoomed view of the part indicated by a red rectangle in Fig. 7(a), showing the transition of modes $HE_{m,37}$, m = 1, 2, …. The dispersion curve of the mode $HE_{m,37}$ changing from a steep slope to a moderate slope indicates the formation of an anti-resonant core-type mode $HE_{m,1+(36)}$ (the nomenclature similar to TE/TM modes). For example, the modes $HE_{1,37}$ at point H1 and $HE_{3,37}$ at point H3 are transferred into the modes $HE_{1,1+(36)}$ at point H2 and $HE_{3,1+(36)}$ at point H4, respectively. Their modal field intensity and electric vector distributions are shown in Fig. 7(c). As the azimuthal mode order 'm' increases, the transition of the cladding-type $HE_{m,37}$ to anti-resonant core-type $HE_{m,1+(36)}$ will occur at a longer wavelength and a smaller effective index at the point where the slope of the dispersion curve changes. Therefore, the transition process for the modes with large azimuthal mode orders 'm' may not be visible in the given range of the dispersion diagram. As an example, although the dispersion curve of the mode $HE_{15,37}$ in Fig. 7(b) intersects the horizontal line corresponding to the value n_1, it does not change direction abruptly, indicating no mode transition in the given range. Two modes at points H5 and H6 on this dispersion curve of the mode $HE_{15,37}$ show similar modal field intensity and electric vector distributions as seen in Fig. 7(c). These two modes are both cladding-type modes with energy confined in the cladding region, however, their formation mechanisms are likely different. Compared to the cladding mode at point H5 with $n_{eff} > n_1$ guided by the total internal reflections at both the inner and outer boundaries of the cladding region, the cladding mode at point H6 with $n_{eff} < n_1$ cannot be guided by the total internal reflections at the inner boundary of the cladding region. The existence of the cladding modes in the dispersion space below the horizontal line at n_1 in Figs. 7(a) and 7(b) is likely attributed to the inhibited coupling effects as per following discussion.

The modal field intensity and electric vector distributions of two anti-resonant core modes $HE_{1,1+(37)}$ at points H7 and H8 are drawn in Fig. 7(c), showing that for both of the modes the field energy is confined in the fiber core region. The intersection of the dispersion curve of

$HE_{1,1+(37)}$ with that of $HE_{15,37}$ indicates that the disc-like core modes and the annular-like cladding modes can exist in the same dispersion space (n_{eff} vs. λ). The same n_{eff} indicates that the modes have the same longitudinal components of the light field. However, they cannot couple with each other since their transverse components of the light field are different, corresponding to the inhibited coupling effect [6].

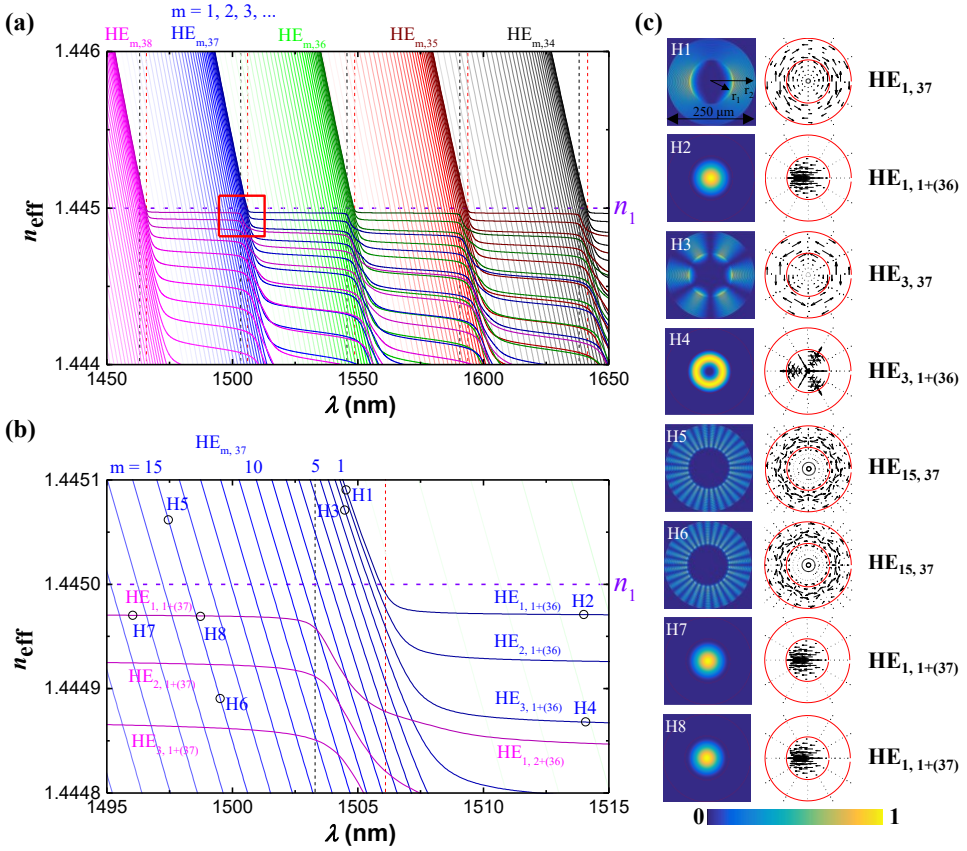

Fig. 7. Dispersion curves (n_{eff} vs. λ) of HE modes with n_{eff} corresponding to (a) n_1-0.001 < n_{eff} < n_1+0.001, n_1 = 1.445. (b) partially enlarged image of (a), indicated by the red frame. (c) shows the modal intensity and electric field vector distributions of HE modes whose positions (n_{eff}, λ) are indicated by the circles in (b). The black and red vertical dashed lines in (a) and (b) indicate the resonant bands.

3.3 Mode degeneracy in DCFs

The dispersion curves of several lower order TE, TM, HE and EH modes in the DCF are drawn together in the same dispersion diagram, shown in Fig. 8(a). Other higher order modes in the DCF are not shown in order to preserve clarity of the diagram. The dispersion diagram shows periodic resonant and anti-resonant bands corresponding to the strong and moderate index dispersion, and the resonant bands are indicated by the black and red vertical dashed lines. Fig. 8(b) displays one of such periodic bands, indicated by the black dashed rectangle. The dispersion curves of the anti-resonant core modes in the DCF such as $\{HE_{1,1+(36)}\}$, $\{TE_{0,1+(36)}$, $HE_{2,1+(36)}$ and $TM_{0,1+(36)}\}$ and $\{EH_{1,1+(36)}$ and $HE_{3,1+(36)}\}$ can be respectively grouped together. In calculation, the longitudinal components of the light field are very small compared to the transverse components of the light field for the anti-resonant core modes. Therefore, the modes in each group can be grouped into a single degenerate scalar mode or a linear polarized mode,

similar to that in the conventional step-index fibers. These degeneracies are broken in the resonant bands, where dispersion curves of TE, TM, HE and EH modes are separated.

If the high-index cladding region is removed, the fiber becomes a conventional step-index fiber, consisting of a bare core and the surrounding air acting as the fiber cladding, where n_{co} = 1.445, n_{cl} = 1, r_{co} = 62.5 um and r_{cl} = ∞. The dispersion curves of the core modes in such a step-index fiber were calculated by graphical method. The vector modes in the obtained fiber such as {$HE_{1,1}$}, {$TE_{0,1}$, $HE_{2,1}$ and $TM_{0,1}$} and {$EH_{1,1}$ and $HE_{3,1}$} can be respectively grouped into linear polarization modes $LP_{0,1}$, $LP_{1,1}$ and $LP_{2,1}$, due to their mode fields being far from cutoff [37, 38]. Fig. 8 shows the dispersion curves of modes $LP_{m,n}$ in the step-index fiber in orange color, which are overlapped with the moderate dispersion curves of the anti-resonant core modes in the DCF. The results indicate that the anti-resonant core modes {$HE_{1,1+(36)}$}, {$TE_{0,1+(36)}$, $HE_{2,1+(36)}$ and $TM_{0,1+(36)}$} and {$EH_{1,1+(36)}$ and $HE_{3,1+(36)}$} in the DCF show similar qualitative and quantitative behaviour with the corresponding core modes {$HE_{1,1}$}, {$TE_{0,1}$, $HE_{2,1}$ and $TM_{0,1}$} and {$EH_{1,1}$ and $HE_{3,1}$} in the conventional step-index fiber. In addition, the effective refractive index of the anti-resonant core modes in the DCF can be approximated as that of the corresponding $LP_{m,n}$ modes in a conventional step-index fiber.

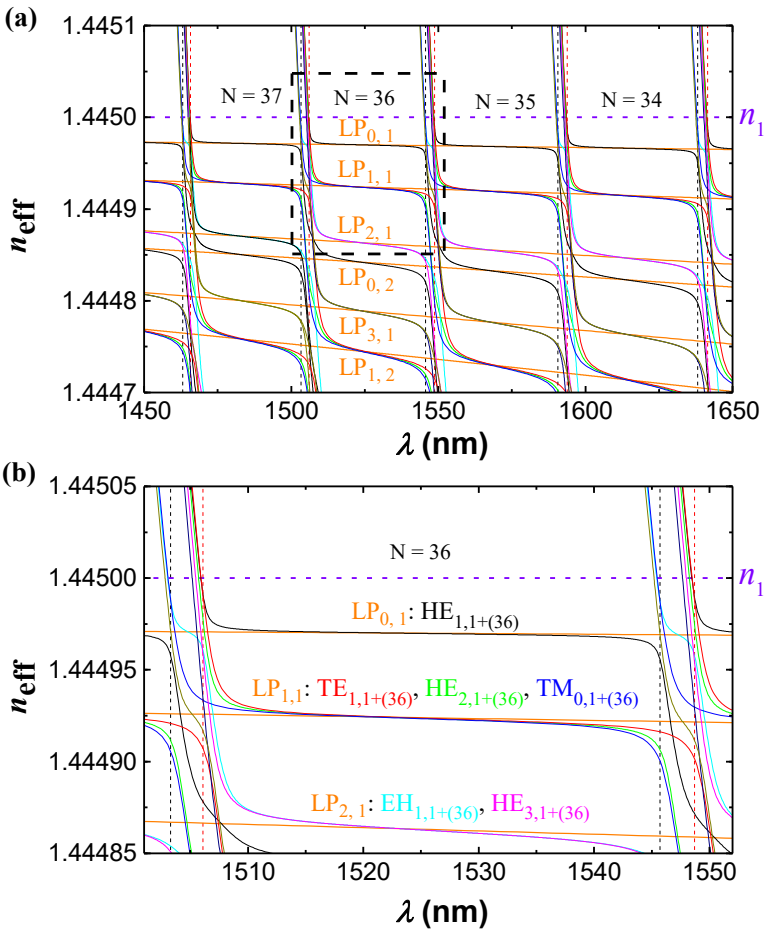

Fig. 8. (a) Dispersion curves (n_{eff} vs. λ) of a depressed core fiber. (b) partially enlarged image of (a), indicated by the black dashed frame. The text labels and the corresponding dispersion curves are of the same color. The orange solid lines in (a) and (b) are for $LP_{m,n}$ modes in a conventional step-index fiber (n_{co} = 1.445, n_{cl} = 1, r_{co} = 62.5 um and r_{cl} = ∞). The black and red vertical dashed lines indicate the resonant bands.

4. Discussion

The dispersion diagram of the DCF shows some similar characteristics with the dispersion diagram of a single-ring hollow-core anti-resonant fiber given in [22]. Firstly, they both show periodic resonant and anti-resonant bands. Secondly, they both show the inhibited coupling phenomenon between the core modes and the cladding modes. However, due to the complex structure of the single-ring hollow-core anti-resonant fibers, only an approximate scalar method was used in [22]. Using the full-vector analytical method in this paper, the transition between the cladding modes and the anti-resonant core modes has been demonstrated. The degeneracy in the anti-resonant bands and the loss of degeneracy around the resonant bands make the dispersion curves of anti-resonant core modes merge together or separate, which may correspond to the narrow and wide variations in bands of anti-resonant modes in [22].

Although the inhibited coupling fiber is different with the photonic bandgap fiber from the modal dispersion perspective, both fibers can be viewed as analogous to the conventional step-index fibers. Ref. [20] shows that the density of core modes in the bandgap fibers is similar to that of the conventional step-index multimode fibers. Our work verified that the density of the anti-resonant core modes in the DCF (a inhibited coupling fiber) is equal to that of the core modes in the equivalent conventional step-index fiber, since the anti-resonant core modes in the former have a one-to-one correspondence to the core modes in the latter.

The core modes in both DCFs and tube-type hollow-core fibers are formed by the anti-resonant effect, yet their properties are different. The n_{eff} of the core modes in DCFs is higher than the refractive index of the surrounding air, therefore they are guided by total internal reflections at the outer boundary of the cladding region and they are non-leaky modes with a real n_{eff}. Compared to the DCFs, the core modes in a tube-type hollow-core fiber are usually treated as leaky modes with a complex n_{eff}. The leaky modes can be solved by the eigenvalue equations in the complex plane, but it is extremely cumbersome. In most of the previous works, only the fundamental mode or a few low-order modes of the hollow-core fibers were obtained with different approximation methods [17, 23-25]. However, the available results for the tube-type hollow-core fibers show some similar characteristics with those for the DCFs. Ref. [17] reports step-like dispersion curves for the modes $HE_{1,n+(N-n)}$ (n = 1, 2, 3, 4, where the radial number 'N-n' in the cladding is not clear), which is similar to the behaviour of the $HE_{1,n+(N-n)}$ modes in the DCFs presented here. Therefore, it can be concluded that all other modes for the tube-type hollow-core fibers are similar to those in DCFs. Since the tube-type hollow-core fiber has a dispersion diagram similar to that of the DCF, the tube-type hollow-core fibers should be considered as inhibited coupling fibers.

The anti-resonance derived anti-crossing phenomenon takes place both in the DCF and in the hollow-core photonics crystal fibers (for either the photonic bandgap guiding or inhibited coupling guiding). The anti-crossing phenomenon has been intensively studied in hollow-core photonic crystal fibers for applications such as generation of the multi-octave supercontinuum [10], ultrafast nonlinear dynamics optics [11] and the broadband robustly single-mode guidance [12]. Therefore, given that DCFs can readily provide manageable waveguide dispersion and exceptional modal field changes, they are worthy further study for a wide range of applications, in addition to the few existing works such as the generation of the supercontinuum [27] and top-hat beams [32]. Furthermore high refractive index coated step-index fibers have been used for sensing of organic vapors, humidity, voltage, pH, and chemical/bio analytes [43] and have a similar refractive index profile to that of DCF which suggests the possibility that DCF might also be useful for sensing. Probably because the thickness of the coating in these structures is small, the inverted refractive index profile and the anti-resonant effect were not observed. Our ongoing works will explore the application of the anti-resonant and inhibited coupling characteristics of the DCFs in optical fiber sensing.

5. Conclusion

DCFs were studied analytically in comparison with the conventional step-index fibers and the tube-type hollow-core fibers and were found to be a form of anti-resonant and inhibited coupling fibers. In this work an asymmetric planar waveguide approach was proposed for the DCFs in the ARROW model. It has been shown that the DCFs support annular-like cladding modes in the tube cladding region and disc-like anti-resonant core modes in the rod core region and both of them were obtained by solving the same group of full-vector eigenvalue equations using the graphical method. The calculated dispersion diagram shows periodic resonant and anti-resonant bands, where the dispersion curves of the anti-resonant core modes intersect with those of the cladding modes. The formation of core-type modes in a low-index core region can be explained by both the anti-resonant and inhibited coupling mechanisms. The anti-resonant core modes exhibit similar qualitative and quantitative behaviors as those of the conventional step-index fibers. The analogy to conventional step-index fibers may provide a convenient tool to model the modes of the DCFs (the inhibited coupling fibers). To the best of our knowledge, it is the first report on the complete vector modal dispersion diagram calculated analytically for an inversed index fiber. Our results can be used to provide a better understanding of the anti-resonant and inhibited coupling guidance mechanisms in complex inversed index fibers such as hollow-core photonic-bandgap fibers, tube-type hollow-core fibers and single-ring hollow-core fibers.

Appendix

Eigenvalue equations for TE, TM, HE and EH modes in DCFs

From the analysis in Section 2, the modes with $n_3 < n_{\text{eff}} < n_1$ are like the cladding modes in three-layer step-index fibers. Therefore, the eigenvalue equations used to calculate the effective refractive index of the modes with $n_3 < n_{\text{eff}} < n_1$ in DCFs is the same as that for the cladding modes in the three-layer stepped-index fibers, as follows [33]:

for the $\text{TE}_{0,\text{N}}$ modes with $n_3 < n_{\text{eff}} < n_1$:

$$\hat{J}\left(Kp_m + \frac{r_m}{\alpha_2 U_2}\right) = \frac{1}{U_2}\left(\hat{K}q_m + \frac{s_m}{\alpha_2 U_2}\right), \text{m} = 0 \tag{2}$$

for the $\text{TM}_{0,\text{N}}$ modes with $n_3 < n_{\text{eff}} < n_1$:

$$\hat{J}\left(\hat{K}p_m + s_{23}\frac{r_m}{\alpha_2 U_2}\right) = \frac{s_{21}}{U_2}\left(\hat{K}q_m + s_{23}\frac{s_m}{\alpha_2 U_2}\right), \text{m} = 0 \tag{3}$$

for the $\text{HE}_{\text{m,N}}$ and the $\text{EH}_{\text{m,N}}$ modes with $n_3 < n_{\text{eff}} < n_1$:

$$\begin{aligned} &p_m^2 + 2\left(\frac{2}{\pi\alpha_2 U_2^2}\right)^2\left(\frac{n_2^2}{n_1 n_3}\right)x_1 x_2 \\ &+ x_1^2 x_2^2\left[\hat{J}\left(\hat{K}p_m + \frac{r_m}{\alpha_2 U_2}\right) - \frac{1}{U_2}\left(\hat{K}q_m + \frac{s_m}{\alpha_2 U_2}\right)\right] \\ &\times\left[\hat{J}\left(\hat{K}p_m + s_{23}\frac{r_m}{\alpha_2 U_2}\right) - \frac{s_{21}}{U_2}\left(\hat{K}q_m + s_{23}\frac{s_m}{\alpha_2 U_2}\right)\right] \\ &= x_1^2\left(\hat{J}p_m - \frac{q_m}{U_2}\right)\left(\hat{J}p_m - s_{21}\frac{q_m}{U_2}\right) + x_2^2\left(\hat{K}p_m + \frac{r_m}{\alpha_2 U_2}\right)\left(\hat{K}p_m + s_{23}\frac{r_m}{\alpha_2 U_2}\right) \end{aligned} \tag{4}$$

The fiber parameters of the DCF shown in Fig. 1 are r_1, r_2, n_1, n_2 and n_3. The wavenumber in vacuum is: $k_0 = 2\pi/\lambda$, where λ is the wavelength. The longitudinal propagation constant is: $\beta = k_0 n_{\text{eff}}$. In the equations (2), (3) and (4), the parameters used are as follows:

$$\alpha_2 = \frac{r_2}{r_1}, \tag{5}$$

$$u_1 = \sqrt{k_0^2 n_1^2 - \beta^2}\,, \tag{6}$$

$$u_2 = \sqrt{k_0^2 n_2^2 - \beta^2}, \tag{7}$$

$$\omega_3 = \sqrt{\beta^2 - k_0^2 n_3^2}\,, \tag{8}$$

$$U_1 = u_1 r_1\,,\ U_2 = u_2 r_1\,,\ W_3 = \omega_3 r_2, \tag{9}$$

$$\hat{J} = \frac{J_m'(U_1)}{U_1 J_m(U_1)}\,, \tag{10}$$

$$\hat{K} = \frac{K_m'(W_3)}{W_3 K_m(W_3)}, \tag{11}$$

$$p_m = J_m(u_2 r_2) Y_m(u_2 r_1) - J_m(u_2 r_1) Y_m(u_2 r_2), \tag{12}$$

$$q_m = J_m(u_2 r_2) Y_m'(u_2 r_1) - J_m'(u_2 r_1) Y_m(u_2 r_2), \tag{13}$$

$$r_m = J_m'(u_2 r_2) Y_m(u_2 r_1) - J_m(u_2 r_1) Y_m'(u_2 r_2), \tag{14}$$

$$s_n = J_m'(u_2 r_2) Y_m'(u_2 r_1) - J_m'(u_2 r_1) Y_m'(u_2 r_2), \tag{15}$$

$$s_{23} = \frac{n_2^2}{n_3^2}, s_{21} = \frac{n_2^2}{n_1^2}, \tag{16}$$

$$V_{12}^2 = k_0^2 r_1^2 (n_1^2 - n_2^2), V_{23}^2 = k_0^2 r_2^2 (n_2^2 - n_3^2), \tag{17}$$

$$x_1^2 = \frac{n_1^2 U_1^4 U_2^4}{\sigma_0^2 V_{12}^4}, x_2^2 = \frac{n_3^2 \alpha_2^4 U_2^4 W_3^4}{\sigma_0^2 V_{23}^4}, \tag{18}$$

$$\sigma_0^2 = \left(\frac{\beta m}{k_0}\right)^2. \tag{19}$$

The parameters u_1, u_2, ω_3, U_1, U_2, W_3 in equations (6)-(9) are phase parameters. The functions J_m, Y_m and K_m in equations (10)-(15) denote the Bessel function of the first kind, the Bessel function of the second kind and the modified Bessel function of the second kind. J_m', Y_m', and K_m' denote the derivatives of the corresponding Bessel functions.

To calculate the TE, TM, HE and EH modes with $n_1 < n_{\text{eff}} < n_2$, the phase parameter u_1 in the equation (6) needs to be modified as:

$$u_1 = \sqrt{\beta^2 - k_0^2 n_1^2} \tag{20}$$

and $\hat{J}$ in the equation (10) need to be modified as:

$$\hat{J} = -\frac{I_m'(U_1)}{U_1 I_m(U_1)}, \tag{21}$$

where I_m and I_m' denote the modified Bessel function of the first kind and its derivative.

The modal intensity and electric field vector distributions can be calculated with the field functions shown in Refs. [33-35].

Funding

This work was supported by the Technological University Dublin under FIOSRAIGH 2016 scholarship program.

Acknowledge

We thank Dr. Cian Taylor from the Institute of Technology Sligo for valuable discussions.

Disclosures

The authors declare that there are no conflicts of interest related to this article.

References

1. S. F. Gao, Y. Y. Wang, W. Ding, D. L. Jiang, S. Gu, X. Zhang, and P. Wang. "Hollow-core conjoined-tube negative-curvature fibre with ultralow loss," Nat. Commun. **9**(1), 1-6 (2018).
2. B. Debord, A. Amsanpally, M. Chafer, A. Baz, M. Maurel, J. M. Blondy, E. Hugonnot, F. Scol, L. Vincetti, F. Gérôme, and F. Benabid, "Ultralow transmission loss in inhibited-coupling guiding hollow fibers," Optica **4**(2), 209-217 (2017).
3. F. Poletti, M. N. Petrovich, and D. J. Richardson. "Hollow-core photonic bandgap fibers: technology and applications," Nanophotonics **2**(5-6), 315–340 (2013).
4. F. Yu and J. C. Knight, "Negative curvature hollow-core optical fiber," IEEE J. Sel. Top. Quantum Electron. **22**, 4400610 (2016).
5. Y. Chen, Z. Liu, S. R. Sandoghchi, G. T. Jasion, T. D. Bradley, E. N. Fokoua, J. R. Hayes, N. V. Wheeler, D. R. Gray, B. J. Mangan, R. Slavík, S. Member, F. Poletti, M. N. Petrovich, S. Member, and D. J. Richardson, "Multi - kilometer long, longitudinally uniform hollow core photonic bandgap fibers for broadband low latency data transmission," J. Lightwave Technol. **34**(4), 104–113 (2016).
6. F. Couny, F. Benabid, P. J. Roberts, P. S. Light, and M. G. Raymer, "Generation and photonic guidance of multioctave optical-frequency combs," Science **318**(5853), 1118–1121 (2007).
7. A. F. Kosolapov, A. D. Pryamikov, A. S. Biriukov, V. S. Shiryaev, M. S. Astapovich, G. E. Snopatin, V. G. Plotnichenko, M. F. Churbanov, and E. M. Dianov, "Demonstration of CO2-laser power delivery through chalcogenide-glass fiber with negative-curvature hollow core," Opt. Express **19**(25), 25723–25728 (2011).
8. A. D. Pryamikov, A. S. Biriukov, A. F. Kosolapov, V. G. Plotnichenko, S. L. Semjonov, and E. M. Dianov, "Demonstration of a waveguide regime for a silica hollow--core microstructured optical fiber with a negative curvature of the core boundary in the spectral region > 3.5 μm," Opt. Express **19**(2), 1441–1448 (2011).
9. P. S. J. Russell, P. Hölzer, W. Chang, A. Abdolvand, and J. C. Travers, "Hollow-core photonic crystal fibres for gas-based nonlinear optics," Nat. Photonics **8**(4), 278–286 (2014).
10. R. Sollapur, D. Kartashov, M. Zürch, A. Hoffmann, T. Grigorova, G. Sauer, A. Hartung, A. Schwuchow, J. Bierlich, J. Kobelke, M. Chemnitz, M. A. Schmidt, and C. Spielmann, "Resonance-enhanced multi-octave supercontinuum generation in antiresonant hollow-core fibers," Light: Sci. Appl. **6**, e17124 (2017).
11. F. Tani, F. Köttig, D. Novoa, R. Keding, and P. S. Russell, "Effect of anti-crossings with cladding resonances on ultrafast nonlinear dynamics in gas-filled photonic crystal fibers," Photon. Res. **6**, 84–88 (2018)
12. P. Uebel, M. C. Günendi, M. H. Frosz, G. Ahmed, N. N. Edavalath, J.-M. Ménard, and P. St. J. Russell, "Broadband robustly single-mode hollow-core PCF by resonant filtering of higher-order modes," Opt. Lett. **41**(9), 1961–1964 (2016).
13. C.-H. Lai, B. You, J.-Y. Lu, T.-A. Liu, J.-L. Peng, C.-K. Sun, and H.-C. Chang, "Modal characteristics of antiresonant reflecting pipe waveguides for terahertz waveguiding," Opt. Express **18**(1), 309–322 (2010).
14. S. Liu, Y. Ji, L. Cui, W. Sun, J. Yang, and H. Li, "Humidity-insensitive temperature sensor based on a quartz capillary anti-resonant reflection optical waveguide," Opt. Express **25**(16), 18929–18939 (2017).
15. D. Liu, Q. Wu, C. Mei, J. Yuan, X. Xin, A. K. Mallik, F. Wei, W. Han, R. Kumar, C. Yu, S. Wan, X. He, B. Liu, G.-D. Peng, Y. Semenova, and G. Farrell, "Hollow Core Fiber Based Interferometer for High Temperature (1000 °C) Measurement," J. Lightwave Technol. **36**(9), 1583–1590 (2018).
16. M. A. Duguay, Y. Kokubun, T. L. Koch, and L. Pfeiffer, "Antiresonant reflecting optical waveguides in SiO2-Si multilayer structures," Appl. Phys. Lett. **49**, 13-15 (1986).
17. J.L. Archambault, R.J. Black, S. Lacroix, and J. Bures, "Loss calculations for antiresonant waveguides," J. Lightwave Technol. **11**, 416-423 (1993).
18. N. M. Litchinitser, A. K. Abeeluck, C. Headley, and B. J. Eggleton, "Antiresonant reflecting photonic crystal optical waveguides," Opt. Lett. **27**(18), 1592–1594 (2002).
19. N. M. Litchinitser, S. C. Dunn, B. Usner, B. J. Eggleton, T. P. White, R. C. McPhedran, and C. M. de Sterke, "Resonances in microstructured optical waveguides," Opt. Express **11**, 1243-1251 (2003).
20. M. J. F. Digonnet, H. K. Kim, G. S. Kino, and S. Fan, "Understanding air-core photonic-bandgap fibers: analogy to conventional fibers," J. Lightwave Technol. **23**, 4169-4177 (2005).
21. K. Z. Aghaie, V. Dangui, M. J. F. Digonnet, S. H. Fan, and G. S. Kino, "Classification of the core modes of hollow-core photonic-bandgap fibers," IEEE J. Quantum Electron. **45**(9), 1192–1200 (2009).
22. R. F. Ando, A. Hartung, B. Jang, and M. A. Schmidt, "Approximate model for analysing band structures of single-ring hollow-core anti-resonant fibers," Opt. Express **27**(7), 10009–10021 (2019).
23. L. Vincetti and V. Setti, "Waveguiding mechanism in tube lattice fibers," Opt. Express **18**(22), 23133–23146 (2010).
24. M. Zeisberger and M. A. Schmidt, "Analytic model for the complex effective index of the leaky modes of tubetype anti-resonant hollow core fibers," Sci. Rep. **7**(1), 11761 (2017).
25. M. Bache, M. S. Habib, C. Markos, and J. Lægsgaard, "Poor-man's model of hollow-core anti-resonant fibers," J. Opt. Soc. Am. B **36**(1), 69–80(2018).
26. V. I. Neves and A. S. C. Fernandes, "Modal characteristics for W-type and M-type dielectric profile fibres", Micro. & Opt. Tech. Lett. **22**, 398-405 (1999)
27. D. Jain, C. Markos, T. M. Benson, A. B. Seddon, and O. Bang. "Exploiting dispersion of higher-order-modes using M-type fiber for application in mid-infrared supercontinuum generation," Sci. Rep. **9**, 8536(2019).
28. M. Hautakorpi and M. Kaivola, "Modal analysis of M-type-dielectric-profile optical fibers in the weakly guiding approximation," J. Opt. Soc. Am. A **22**(6), 1163–1169 (2005).

29. A. S. Belanov and S. V. Tsvetkov, “High-index-ring three-layer fibres for mode-locked sub-1.3 μm fibre lasers,” Quantum Electron. **40**(2), 160–162 (2010).
30. S. S. Aleshkina, M. E. Likhachev, A. K. Senatorov, M. M. Bubnov, M. Y. Salaganskii, and A. N. Guryanov. "Low-loss hybrid fiber with zero dispersion wavelength shifted to 1 μm." Opt. express **21**(20), 23838-23843 (2013).
31. S. S. Aleshkina, M. V. Yashkov, M. M. Bubnov, A. N. Guryanov, and M. E. Likhachev. "Asymptotically single-mode hybrid fiber for dispersion management near 1 μm." IEEE J. Sel. Topics Quantum Electron **24**(3) 1-8(2017).
32. C. Valentin, P. Calvet, Y. Quiquempois, G. Bouwmans, L. Bigot, Q. Coulombier, M. Douay, K. Delplace, A. Mussot, and E. Hugonnot, “Top-hat beam output of a single-mode microstructured optical fiber: Impact of core index depression,” Opt. Express **21**(20), 23250–23260(2013).
33. C. Tsao, *Optical Fibre Waveguide Analysis* (Oxford University Press, New York, 1992).
34. T. Erdogan, “Cladding-mode resonances in short- and long-period fiber grating filters,” J. Opt. Soc. Am. A **14**, 1760-1773 (1997).
35. Z. Zhang and W. Shi, “Eigenvalue and field equations of three-layered uniaxial fibers and their applications to the characteristics of long-period fiber gratings with applied axial strain,” J. Opt. Soc. Am. A **22**, 2516–2526 (2005)
36. D. Marcuse, *Theory of Dielectric Optical Waveguides*, *2nd ed.* (Academic, New York, 1991).
37. X. K. Lian, G. Farrell, Q. Wu, W. Han, F. F. Wei, and Y. Semenova. "Mode Transition in Conventional Step-Index Optical Fibers." in 2019 18th International Conference on Optical Communications and Networks (ICOCN), (IEEE, 2019), pp. 1-3.
38. X. K. Lian, Q. Wu, G. Farrell, C. Y. Shen, Y. Q. Ma, and Y. Semenova. "Discrete self-imaging in small-core optical fiber interferometers." J. Lightwave Technol. **37**(9), 1873-1884 (2019).
39. M. Born, and E. Wolf. *Principles of Optics* (Cambridge University Press, 1999).
40. I. Del Villar, I. R. Matías, F. J. Arregui, and P. Lalanne, “Optimization of sensitivity in Long Period Fiber Gratings with overlay deposition,” Opt. Express **13**, 56-69 (2005).
41. A. Cusano, A. Iadicicco, P. Pilla, L. Contessa, S. Campopiano, A. Cutolo, and M. Giordano, “Mode transition in high refractive index coated long period gratings,” Opt. Express **14**(1), 19–34 (2006).
42. L. L. Xue and Y. Li, “Sensitivity enhancement of RI sensor based on SMS fiber structure with high refractive index overlay,” J. Lightwave Technol. **30**(10), 1463–1469 (2012).
43. I. Del Villar, F. J. Arregui, C. R. Zamarreño, J. M. Corres, C. Bariain, J. Goicoechea, C. Elosua, M. Hernaez, P. J. Rivero, A. B. Socorro, A. Urrutia, P. Sanchez, P. Zubiate, D. Lopez, N. De Acha, J. Ascorbe, and I. R. Matias, “Optical sensors based on lossy-mode resonances,” Sens. Actuators B Chem. **240**, 174–185 (2017).